FULL PAPER

Synthesis of Layer-Tunable Graphene: A Combined Kinetic Implantation and Thermal Ejection Approach

Gang Wang, Miao Zhang, Su Liu, Xiaoming Xie, Guqiao Ding, Yongqiang Wang, Paul K. Chu, Heng Gao, Wei Ren, Qinghong Yuan, Peihong Zhang, Xi Wang, and Zengfeng Di**

Layer-tunable graphene has attracted broad interest for its potentials in nanoelectronics applications. However, synthesis of layer-tunable graphene by using traditional chemical vapor deposition method still remains a great challenge due to the complex experimental parameters and the carbon precipitation process. Herein, by performing ion implantation into a Ni/Cu bilayer substrate, the number of graphene layers, especially single or double layer, can be controlled precisely by adjusting the carbon ion implant fluence. The growth mechanism of the layer-tunable graphene is revealed by monitoring the growth process, it is observed that the entire implanted carbon atoms can be expelled toward the substrate surface and thus graphene with designed layer number can be obtained. Such a growth mechanism is further confirmed by theoretical calculations. The proposed approach for the synthesis of layer-tunable graphene offers more flexibility in the experimental conditions. Being a core technology in microelectronics processing, ion implantation can be readily implemented in production lines and is expected to expedite the application of graphene to nanoelectronics.

1. Introduction

Graphene is a promising material in nanoelectronics and flexible electronic devices due to its unique 2D hexagonal lattice structure and extraordinary physical properties.[1–4] To realize the potential of graphene in nanoelectronic devices, a uniform graphene layer with a well-controlled layer number should be synthesized first because most of the physicochemical properties of graphene are sensitive to its thickness. For example, monolayer graphene has a zero band gap, whereas Bernal-stacked (AB-stacked) bilayer graphene is of significant interest for graphene-based field-effect transistors (FETs) and tunable laser diodes,[5–7] because of the feasibility to continuously tune up its band gap to 250 mV by applying a perpendicular electric field. However, precise control of the thickness of graphene remains a major challenge. For the carbon-soluble materials (e.g., Ni,[8] Co,[9] Ru,[10] Pd,[11] and Mo[12]), the chemical vapor deposition (CVD) synthesis of graphene proceeds via surface segregation followed by precipitation. Since the precipitation process is nonequilibrium, it is extremely challenging to tune the layer number of graphene using carbon-soluble metals in theory, though several approaches have attempted by reducing metal film thickness

Dr. G. Wang, Prof. M. Zhang, Prof. X. Xie, Prof. G. Ding, Prof. X. Wang, Prof. Z. Di
State Key Laboratory of Functional Materials for Informatics
Shanghai Institute of Microsystem and Information Technology
Chinese Academy of Sciences
865 Changning Road, Shanghai 200050, P. R. China
E-mail: zfdi@mail.sim.ac.cn
Dr. G. Wang, Prof. S. Liu
School of Physical Science and Technology
Lanzhou University
Lanzhou 730000, P. R. China
Prof. Y. Wang
Materials Science and Technology Division
Los Alamos National Laboratory
Los Alamos, NM 87545, USA
Prof. P. K. Chu
Department of Physics and Materials Science
City University of Hong Kong
Tat Chee Avenue, Kowloon, Hong Kong 999077, China
Dr. H. Gao, Prof. W. Ren, Prof. P. Zhang
International Centre for Quantum and Molecular Structures and Department of Physics
Shanghai University
99 Shangda Road, Shanghai 200444, China
Prof. Q. Yuan
Department of Physics
East China Normal University
500 Dongchuan Road, Shanghai 200241, China
E-mail: qhyuan@phy.ecnu.edu.cn
Prof. P. Zhang
Department of Physics
University at Buffalo
State University of New York
Buffalo, NY 14260, USA

DOI: 10.1002/adfm.201500981

or controlling the cooling rate. In contrast, for the carbon-insoluble materials (e.g., Cu,[13] Pt,[14] Ag,[15] Ir,[16] and Ge[17]), graphene growth by CVD proceeds through a surface mechanism that is self-limiting, yielding film with essentially monolayer of graphene, but incapable of producing the graphene with multiple layers. Furthermore, by combining the virtues of carbon-soluble and carbon-insoluble materials, Ni–Cu,[18,19] Ni–Mo,[20] Co–Cu,[21] Ni–Au[22] binary alloys and Ni/Cu bilayered substrate called smart Janus substrates have been reported as excellent platforms to control the layer number of graphene synthesized by CVD. However, even for the smart Janus substrates, the ability of controlling the layer number of graphene films is still limited, since both carbon absorption and carbon precipitation processes are thermally driven and occur simultaneously,[23–25] and it is unable to achieve satisfactory decoupling of them.

Other than the carbon absorption process of CVD growth, the carbon introduction process by ion implantation is a non-equilibrium process and not thermally driven, so it is well decoupled from the final carbon precipitation process. Furthermore, as a mature technology in the microelectronic industry, ion implantation has the preeminent advantage in the control of the content of doping species, i.e., carbon atoms. Therefore, in recent years, ion implantation method has been proposed to control the layer number of graphene on single metal substrate, such as Ni[26–28] and Cu,[29] but the advantage seems not prominent due to the limitation of the single metal substrate. For example, the thickness of graphene on the Ni substrate is nonuniform and the correlation between the carbon-implant fluence and layer number of graphene is not strictly followed, although the average graphene thickness is determined roughly by the carbon ion fluence.[30] With respect to the Cu substrate, the thickness of graphene does not vary and bilayer graphene with good uniformity always form in spite of substantial variation in the carbon ion fluence.[29] However, to our best knowledge, the use of dual metal substrate combined with ion implantation for the synthesis of layer-tunable graphene has never been explored.

Herein, by taking advantage of the dual metal substrate of the Ni-coated Cu foils,[25] the precise control of layer number of graphene by ion implantation has been demonstrated and the layer number of graphene strictly corresponds to the implantation fluence as expected. For instance, uniform monolayer graphene can be produced using a fluence of 4×10^{15} atoms cm^{-2}, and a fluence of 8×10^{15} atoms cm^{-2} produces a bilayer graphene film. In addition, different from previous reports where carbon atoms are precipitated through cooling, the precipitation of carbon in our work is achieved under steady temperature, which is benefit to the defect healing of graphene and leads to the formation of graphene layers with excellent crystalline and uniformity. The formation mechanism is explored and confirmed by theoretical calculation. Superior to CVD method, our approach is less sensitive to the processing conditions, especially the thermal history, since the carbon content is solely determined by the implantation fluence. Given that the ion implantation is a mature technology in the current integrated circuit manufacturing, we believe that graphene synthesized by this strategy can expedite the industrial application of graphene.

2. Results and Discussions

Figure 1 illustrates the graphene synthesis process. The Ni/Cu bilayer substrate, which is fabricated by the deposition of 300 nm Ni layer on top of Cu foil, is implanted at room temperature with 60 keV carbon ions with the predetermined fluence. According to the SRIM Monte Carlo code,[31] the projected range of the implanted ions in Ni is about 70 nm with a spread of 41 nm. The fluence of implanted ions can be precisely controlled by means of a Faraday cup, and the fluences of 4×10^{15} and 8×10^{15} atoms cm^{-2} are adopted to obtain uniform monolayer and bilayer graphene films, respectively. The graphene film with the desired layer number is achieved after the thermal treatment of implanted Ni/Cu bilayer substrate, as described in Figures S1–S4 (Supporting Information).

Figure 2 depicts the Raman spectra of the graphene films fabricated on the Ni/Cu bilayer substrate showing three primary peaks, D band at ≈1350 cm^{-1}, G band at ≈1580 cm^{-1}, and 2D band at ≈2700 cm^{-1}. The relatively low intensity of the D band suggests that the as-synthesized graphene film possesses excellent crystalline quality comparable to that of the conventional CVD graphene.[32,33] The number of layers is determined by the intensity ratio of the 2D to G peak (I_{2D}/I_G) and the full-width at half-maximum (FWHM) of the symmetric 2D band. For a fluence of 4×10^{15} atoms cm^{-2}, the I_{2D}/I_G ratio is larger than 1.5, indicating that a monolayer graphene film is formed. Similar to the reported single-layer graphene,[20] the symmetrical 2D band with an FWHM of ≈30 cm^{-1} can be fitted by a single Lorentzian curve, as shown in the inset of Figure 2a. For the sample synthesized with the fluence of 8×10^{15} atoms cm^{-2}, the corresponding I_{2D}/I_G value decreases to about 0.5 and the symmetrical 2D band with an FWHM of ≈45 cm^{-1} can be fitted by four Lorentzian curves, as shown in the inset of Figure 2d. These features clearly indicate the formation of bilayer graphene.[34] The thickness of the graphene films is further corroborated by UV–visible spectrophotometry, since the absorbance of the single graphene layer is 2.3%.[35] From the comparison of absorbance, it is shown that the absorbance of the bilayer graphene is twice that of the monolayer graphene (Figure S5a,b, Supporting Information). The thicknesses measurements by atomic force microscopy (AFM) provide further evidence of the monolayer and bilayer structures, as shown in Figure S5c,d (Supporting Information), respectively. Moreover, the synthesis of trilayer graphene by carbon ion implantation (fluence of 1.2×10^{16} atoms cm^{-2}) into the Ni/Cu bilayer substrate is also conducted, and the formation of trilayer graphene is evident by the symmetrical 2D band with an FWHM of ≈79 cm^{-1}, which can be fitted by six Lorentzian curves, as reported by Sun et al.[36] However, the thickness uniformity and crystalline quality still need improvement by tuning the experimental conditions, as shown in Figure S6 (Supporting Information).

In order to further investigate their microscopic structures, the monolayer graphene and the bilayer graphene are characterized by scanning tunneling microscopy (STM). Figure 2b,e displays the microscopic structures of the synthesized monolayer and bilayer graphene, respectively. As shown by the magnified image in the inset of Figure 2b, a typical honeycomb lattice structure is observed from the monolayer graphene.[37] With regard to the bilayer graphene, the honeycomb lattice

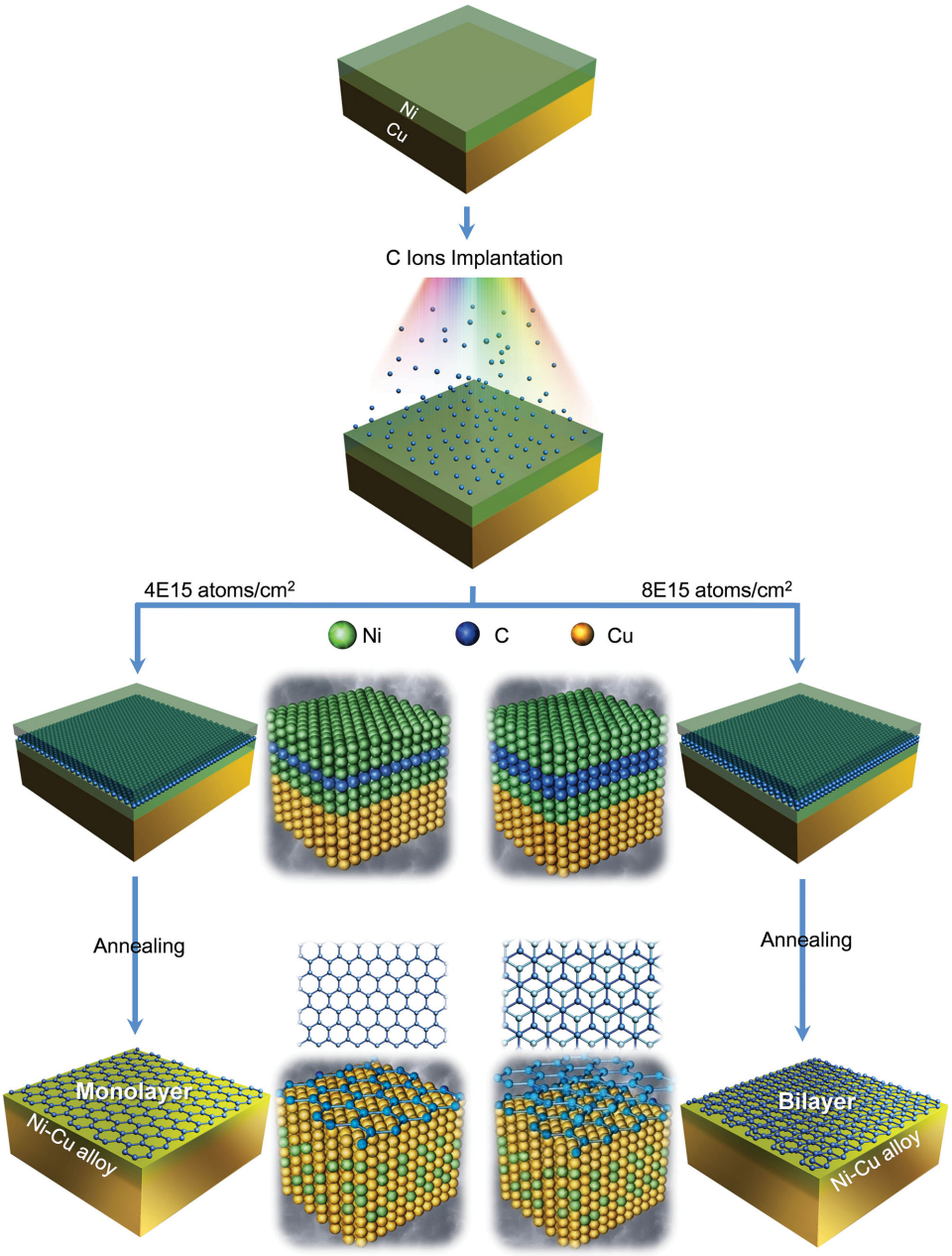

Figure 1. Schematic diagrams showing the synthesis process of monolayer and bilayer graphene by ion implantation. Carbon ions with the predesigned fluence (the fluences of 4×10^{15} and 8×10^{15} atoms cm^{-2} correspond to the amount of carbon atoms in a monolayer and a bilayer graphene film, respectively) were implanted into the top Ni layer of the Ni/Cu bilayer substrate followed by annealing under H_2 and Ar gas flow. The thermal process initiates interdiffusion of Cu atoms and Ni atoms to form the Cu like alloy. Carbon atoms are expelled from the Cu-like alloy toward the surface and graphene with the expected layer number is formed on the surface.

transforms into a structure with a threefold symmetry, which is a representative structure of the AB-stacked bilayer graphene,[38] as shown in the inset of Figure 2e. These two STM images show few to no defects in a range greater than 100 nm^2, indicating the high crystalline quality of both the monolayer and bilayer graphene. Raman mapping is conducted in a 12 × 12 μm^2 area with a spot size of 1 μm and step size of 1 μm to confirm the thickness uniformity of the graphene films. In a typical monolayer graphene film (shown in Figure 2c), more than 95% of the graphene area have I_{2D}/I_G ratios larger than 1.25. However, in Figure 2f, no monolayer Raman signature ($I_{2D}/I_G > 1.25$) is observed at any pixel on the map and ≈90% of the film have an I_{2D}/I_G ratios of 0.3–0.6, suggesting the formation of uniform bilayer graphene. Furthermore, the excellent uniformity can be achieved from even larger area (Figure S7, Supporting Information).

Transmission electron microscopy (TEM) and selected area electron diffraction (SAED) patterns are powerful tools

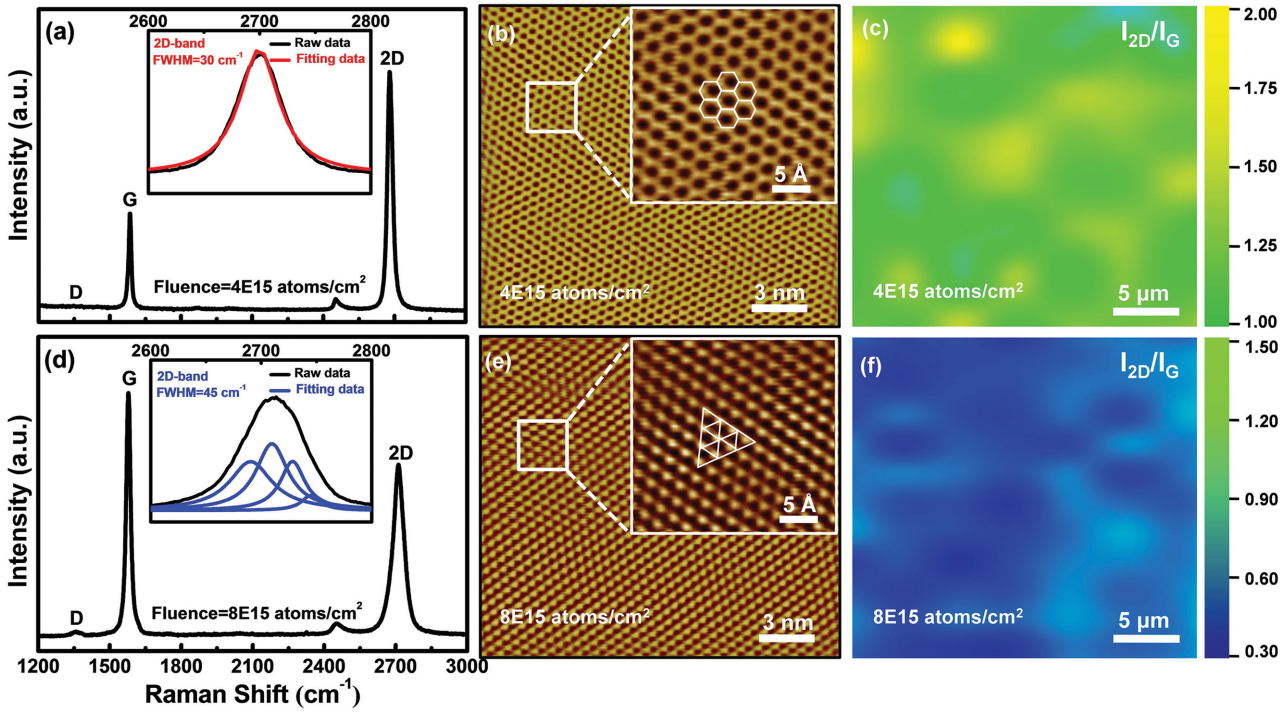

Figure 2. Characterization of monolayer and bilayer graphene synthesized by carbon ion implantation (fluences of 4×10^{15} and 8×10^{15} atoms cm^{-2}) into the Ni/Cu bilayer substrate. a,d) Raman spectra of the monolayer and bilayer graphene, respectively, with the inset in each figure showing the FWHM and Lorentzian fitting of the 2D band. b,e) STM topographical images of the monolayer and bilayer graphene, respectively; the inset in each figure corresponds to the selected region with a higher magnification. c,f) I_{2D}/I_G peak ratio derived from Raman mapping conducted on the monolayer and bilayer graphene, respectively.

to impart the crystallographic information of graphene film including thickness, domain size, and stacking order.[36] Plan-view TEM images shown in **Figure 3**a1,b1 indicate that both monolayer and bilayer graphene films are continuous over a large area. High-resolution TEM (Figure 3a3,b3) obtained from the crack edges of the monolayer and bilayer graphene films (Figure 3a2,b2) exhibit the single layer and bilayer characteristics, respectively. The SAED pattern (Figure 3a4) exhibits only one set of hexagonal diffraction pattern, and the band intensity ratio (outermost to innermost) of ≈1:2 (Figure 3a5) suggests the formation of single-layer graphene. The hexagonal diffraction pattern is also observed as the implantation fluence increases from 4×10^{15} to 8×10^{15} atoms cm^{-2}, however, the band intensity ratio changes to ≈2:1 (Figure 3b5) indicates the formation of AB-stacked bilayer graphene, as reported by others.[21,25,32,36,39] To investigate the spatial crystallographic orientation of graphene, extensive SAED patterns (Figure S8a,b, Supporting Information) were collected at the different locations, as summarized in Figure 3a1,b1 as well. For the single layer graphene, most of the measured area shares a preferential crystal orientation within a ±3° range, indicating the presence of graphene domain with considerable size.[40] However, the crystalline quality for bilayer graphene degrades a little bit, as evidenced by the presence of orientation other than the preferential crystal orientation. Furthermore, non-AB-stacked bilayer graphene domain is occasionally observed, as suggested by the existence of two sets of hexagonal diffraction patterns.

In order to fathom the formation process of uniform monolayer and bilayer graphene on the Ni/Cu bilayer substrate by carbon ion implantation, multifaceted characterization of the samples is performed at different stages. To monitor the status in each stage, secondary ion mass spectrometry (SIMS) is used to determine the Ni, Cu, and carbon depth profiles in the Ni/Cu bilayer substrate and X-ray photoelectron spectroscopy (XPS) analysis is performed to measure the surface chemical composition and chemical states (Table S1, Supporting Information), as shown in **Figure 4**. After carbon ion implantation into the top Ni layer of the Ni/Cu bilayer substrate at room temperature, the implanted carbon ion, which acts as a carbon reservoir for subsequent synthesis of graphene, shows a Gaussian-like distribution in the top Ni layer, as shown in Figure 4a1 [Note that the carbon concentration is plotted on a linear scale (left vertical axis) whereas the Ni and Cu contents are on a logarithmic scale (right vertical axis)]. Since the implantation energy can be tailored to ensure that the implanted ions come to rest in the top Ni layer, the abrupt interface between Ni and Cu is not perturbed and the heterostructured Ni/Cu bilayer substrate is intact after carbon ion implantation, as schematically illustrated in the inset of Figure 4a1. It should be noted that carbon ion implantation is a nonequilibrium process and the amount of carbon atoms introduced by ion implantation can be easily tuned by the implantation fluence thus providing a flexible parameter to tune the thickness of graphene. This is quite different from the conventional CVD approach. The XPS results shown in Figure 4b1 indicate that only Ni signal is found near

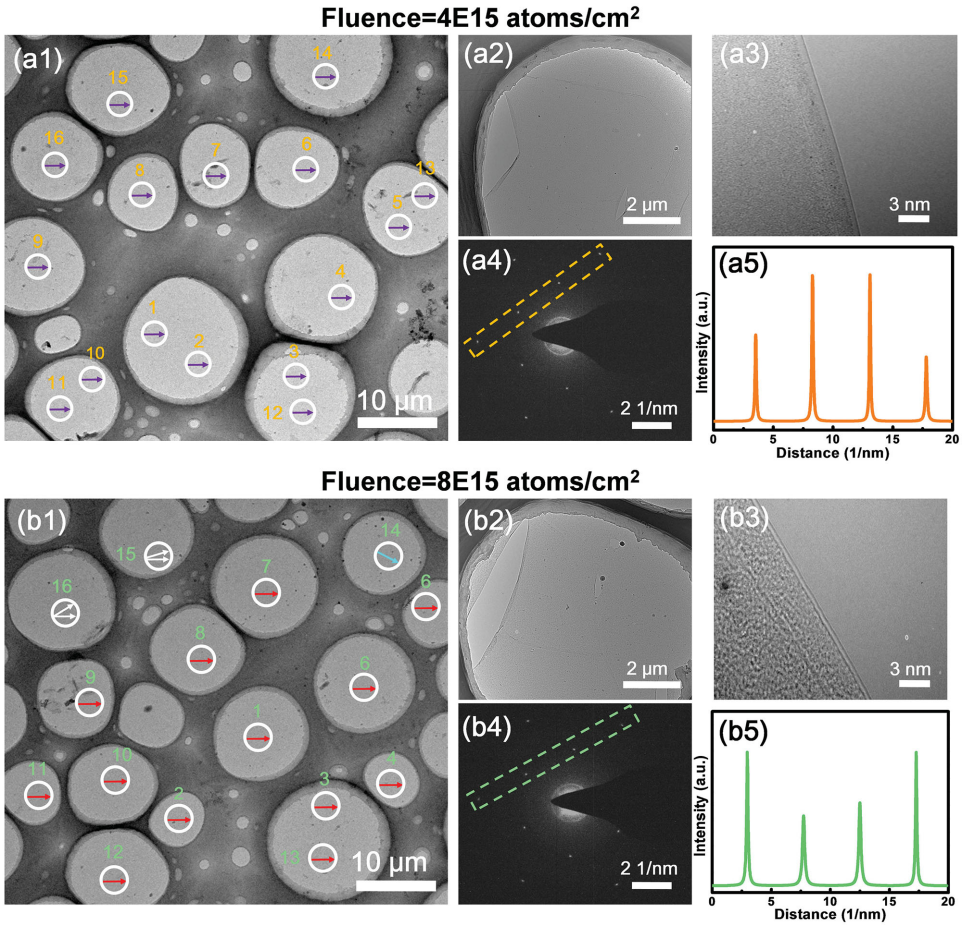

Figure 3. Montage of TEM, HRTEM, and SAED pattern showing the crystallographic information of monolayer and bilayer graphene films including thickness, domain size, and stacking order. a1,b1) Plan view TEM images showing the continuity of the monolayer and bilayer graphene films over a large area, respectively. The numbered white circles indicate different locations where SAED patterns are obtained. Arrows in different colors represent the orientation of the graphene grains in the selected locations normalized with respect to that at location 1. a2,b2) TEM image of monolayer and bilayer graphene cracks on the grids, respectively. a3,b3) HRTEM image of monolayer and bilayer graphene, respectively. a4,b4) SAED patterns of monolayer and bilayer graphene, respectively. a5,b5) Profiles of diffraction spot intensities along box in (a4) and (b4), respectively.

the surface in addition to natural carbon and oxygen surface contamination. Deconvolution of the high-resolution C-1s spectra (inset, Figure 4b1) shows a main carbon sp^3-hybridization peak located at 285.1 eV and a minor sp^2-hybridization peak at 284.6 eV. These results confirm the presence of natural carbon contamination.[41]

After annealing at 950 °C for 3 min, interdiffusion near the interface of Ni/Cu bilayer substrate commences and the thickness of the (pure) Ni film on the top layer decreases due to out-diffusion of Cu, as shown in Figure 4a2. As a consequence of carbon atoms diffusion, the implanted carbon atoms tend to become more uniformly distributed (Figure 4a2) in the Ni layer. Redistribution of carbon is a result of the enhanced diffusivity of carbon in Cu/Ni at elevated temperature and will be discussed in more details later. The XPS data in Figure 4b2 indicates no noticeable change in the surface chemical composition with the exception of a small increase in the intensity of the C1s peak and sp^2 component of the C—C bonds. Therefore, this stage is characterized by Ni/Cu interdiffusion and carbon redistribution, as shown in the inset of Figure 4a2.

Further annealing for three more minutes (6 min total), Ni/Cu interdiffusion becomes more apparent. The top Ni layer is gradually transformed into the Cu–Ni alloy with a small fraction of the Cu component, as shown in Figure 4a3. Formation of Cu–Ni alloy is also confirmed by Cu showing up near the surface (Figure 4b3). It is well known that Ni has a moderate carbon solubility of 0.4–2.7 at% between 700 and 1300 °C, whereas the solubility of carbon in Cu is extremely low (<0.004 at%) at 1000 °C.[42] Therefore, the carbon solubility in the newly formed alloy may decrease substantially as interdiffusion of Ni and Cu proceeds to form the Cu–Ni alloy. In this stage, the carbon atoms are mainly homogeneously distributed in the newly formed Cu–Ni alloy, as shown in Figure 4a3, but the total amount of carbon atoms is reduced compared to the as-implanted sample. Owing to the reduced solubility of carbon in the newly formed Cu–Ni alloy, the implanted carbon ions are gradually expelled to the surface and transformed into graphene, as evidenced by the dominant sp^2 component in the inset of Figure 4b3.

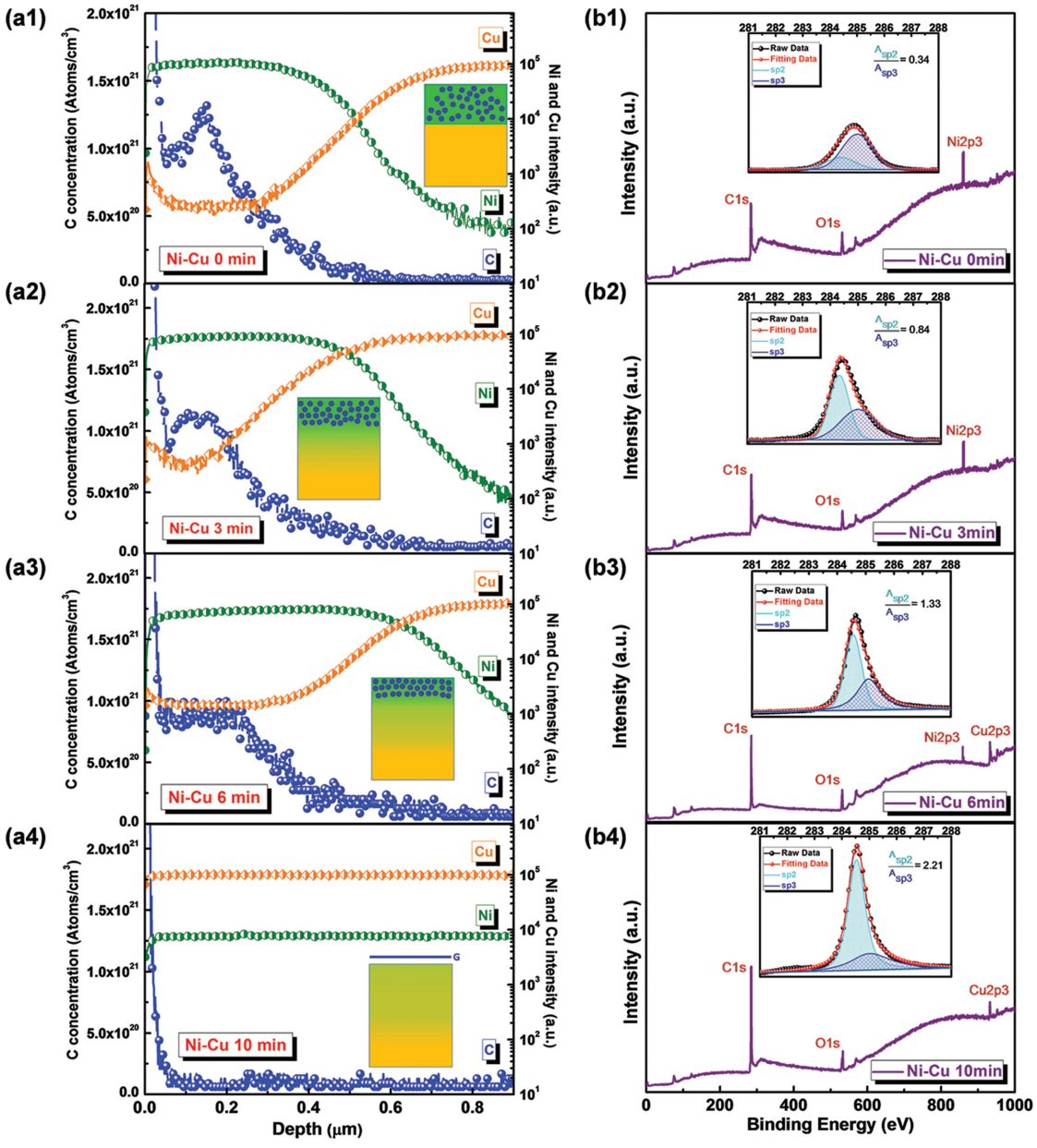

Figure 4. SIMS depth profiles of Cu, Ni, and C in C-implanted Ni/Cu bilayer substrate after annealing for: a1) 0 min; a2) 3 min; a3) 6 min; and a4) 10 min. The inset in each figure shows a schematic illustration of the formation process of graphene by carbon ion implantation into the Ni/Cu bilayer substrate. XPS analysis of the surface chemical composition of C-implanted Ni/Cu bilayer substrate after annealing for: b1) 0 min; b2) 3 min; b3) 6 min; and b4) 10 min. Each inset depicts the chemical states of the C–C bonds. Here, A_{sp2} / A_{sp3} stands for the area ratio between the sp^2-hybridized C—C bonds and the sp^3-hybridized C—C bonds.

Since the Cu substrate can be considered infinitely thick relative to the top Ni layer, as Ni/Cu interdiffusion proceeds, the thin Ni film will be diluted by Cu and eventually, the top Ni layer morphs completely into the Cu-like alloy (Figure 4a4). The concentration of Ni is well below the detection limit of XPS, as shown in Figure 4b4. As the solubility of carbon in the formed Cu-like alloy is extremely low, all the implanted carbon ions are expelled to the surface (assisted by the enhanced carbon diffusivity) to form graphene, as depicted in Figure 4a4. In addition to the disappearance of the Ni signal, the XPS peaks corresponding to both C1s and Cu2p[3] are significantly enhanced at the surface. The high-resolution C1s signal (inset of Figure 4b4) shows that the peak consists of predominantly sp^2 hybridization, indicating that the formation of sp^2 network, i.e., graphene, on the surface.

Based on the above analysis, it can be concluded that the formation of graphene is attributed to the rejection of implanted carbon atoms driven by Cu–Ni alloying during annealing. To further confirm the mechanism, first-principles calculation is performed to evaluate the stability of carbon in the Cu–Ni alloy with

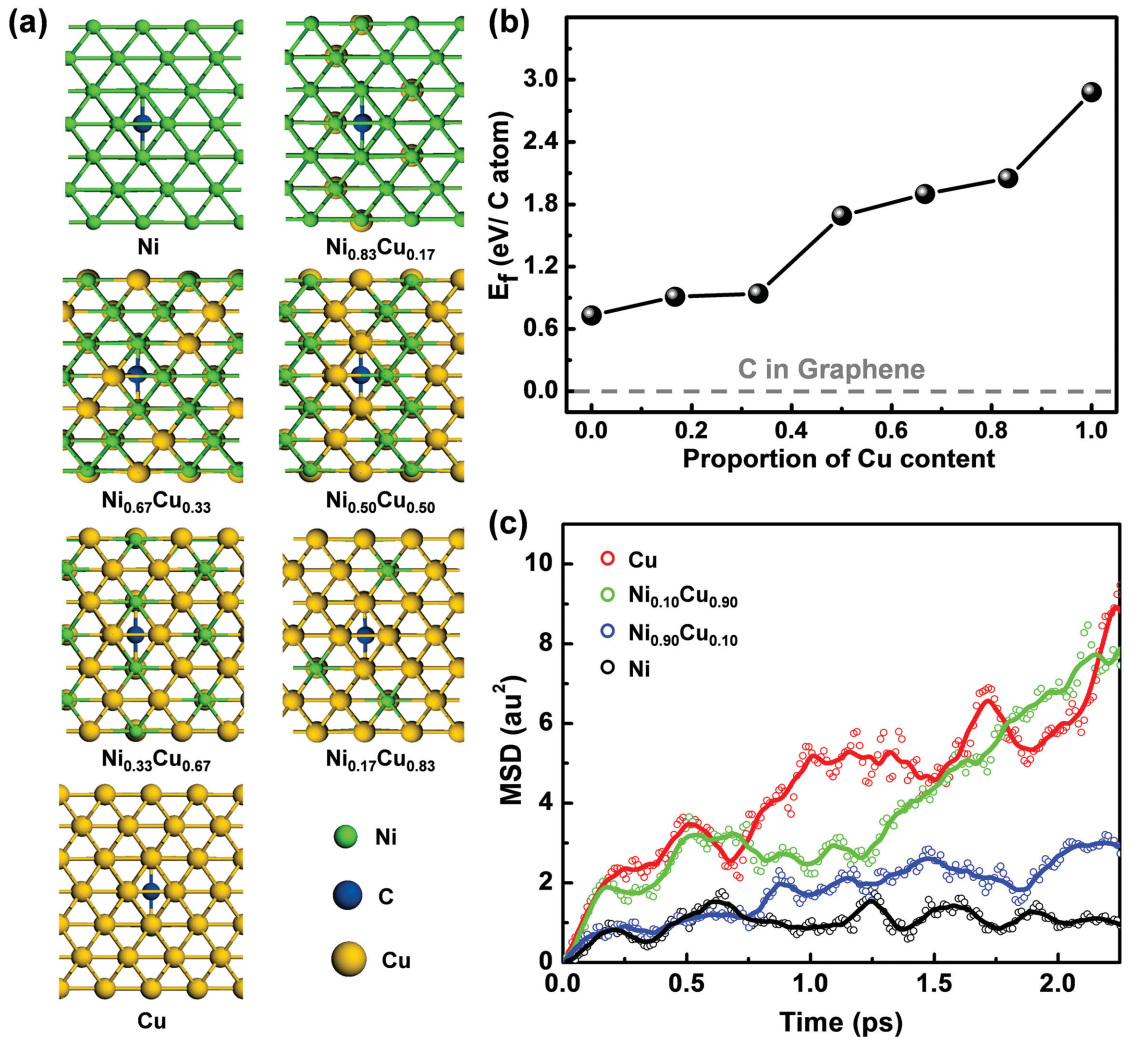

Figure 5. Theoretical calculations on stability and diffusion of C dissolved in Cu–Ni alloy. a) Proposed model for the formation energy of carbon atom in Cu–Ni alloys with different Cu concentrations. b) Formation energy (E_f) profile of carbon atom dissolved in Cu–Ni alloys with different Cu component. The formation energy of carbon atom increases from 0.73 to 2.88 eV with increasing Cu content in the Cu–Ni alloy from 0.0 (pure Ni) to 1.0 (pure Cu). c) Mean squared displacement of carbon atoms in Cu (red), Cu-rich Cu–Ni alloy ($Ni_{0.10}Cu_{0.90}$) (green), Ni-rich Cu–Ni alloy ($Ni_{0.90}Cu_{0.10}$) (blue), and Ni (black). (The solid lines are guides to the eye.)

different Cu/Ni ratios using formation energy as a measure. The formation energy (E_f) of carbon in the substrate is defined as

$$E_f = E_{C+S} - E_S - E_{C@G} \quad (1)$$

where E_{C+S} is the energy of the metal substrate with dissolved carbon atoms, E_S is the energy of the substrate without carbon atoms, and $E_{C@G}$ is the energy of a carbon atom in graphene. All the quantities are properly normalized with respect to the number of atoms in the systems.

Seven substrates with different Cu concentrations of 0%, 17%, 33%, 50%, 67%, 83%, and 100% are explored and the proposed model is shown in **Figure 5**a. With increasing Cu content, the carbon formation energy E_f increases monotonically (Figure 5b). For example, the formation energy of carbon in bulk Ni is about 0.73 eV, whereas that in bulk Cu is 2.88 eV. As Cu atoms diffuse into the Ni film to form the Cu-rich alloy, the formation energy E_f of the implanted carbon atoms increases rapidly. Therefore, it is thermodynamically more favorable for these carbon atoms to move from the Cu-rich part to the Ni-rich part and finally precipitate on the surface to form graphene.

Precipitation of carbon is only possible if the process is kinetically feasible. To illustrate that the diffusivity of carbon is indeed greatly enhanced in Cu/Ni, first-principles molecular dynamics (MD) simulation is conducted. Diffusion of carbon atoms in four representative systems is performed, namely, bulk Ni, bulk Cu, $Ni_{0.90}Cu_{0.10}$ alloy, and $Ni_{0.10}Cu_{0.90}$ alloy at an elevated temperature of 1000 K. Figure 5c shows the mean-squared displacement (MSD) of carbon atoms in these systems. Although carbon atoms essentially do not diffuse away from their local equilibrium positions in bulk Ni, the diffusivity is enhanced in the $Ni_{0.90}Cu_{0.10}$ alloy and carbon atoms in both the bulk Cu and $Ni_{0.10}Cu_{0.90}$ alloy are highly diffusive in this temperature range. These results further confirm that carbon

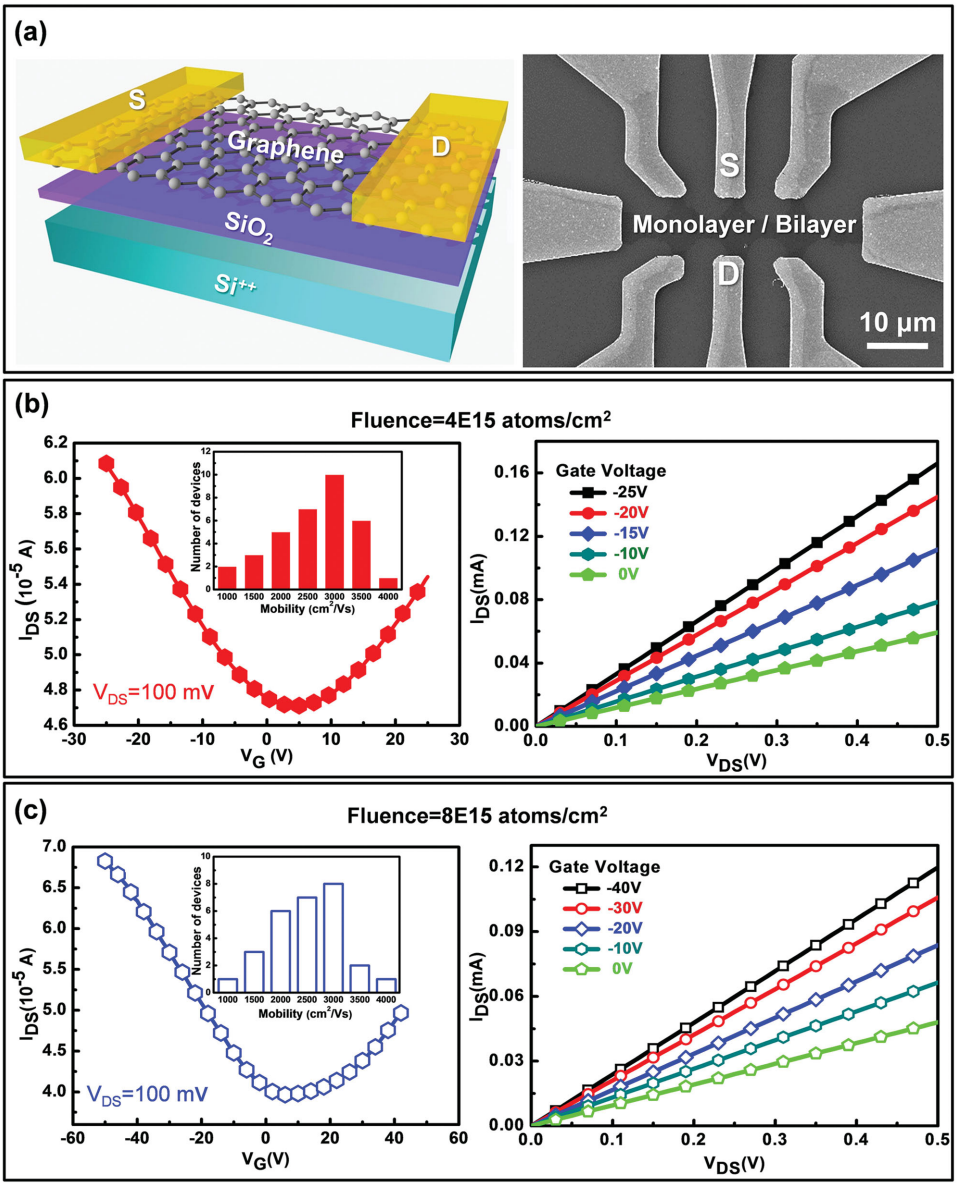

Figure 6. Electrical properties of the monolayer and bilayer graphene. a) Schematic diagram and a SEM image of the fabricated GFET device. b) Transfer (I_{DS} - V_G) (left panel) and output (I_{DS} - V_{DS}) (right panel) characteristics of the monolayer graphene synthesized by carbon ion implantation with a fluence of 4×10^{15} atoms cm^{-2}. The inset in left panel shows histogram of the field effect mobility distribution for total 28 devices. c) Transfer (I_{DS} - V_G) (left) and output (I_{DS} - V_{DS}) (right) characteristics of the bilayer graphene synthesized by carbon ion implantation with a fluence of 8×10^{15} atoms cm^{-2}. The inset in left panel shows histogram of the field effect mobility distribution for total 28 devices.

atoms become increasingly mobile as Ni/Cu interdiffusion proceeds. Ultimately, the carbon atoms precipitate on the substrate surface to form graphene. Formation of graphene assisted by the well-known catalytic effects of the substrate is ultimately determined by thermodynamics as discussed previously.

Unlike the conventional CVD technique to prepare graphene on Ni–Cu, Ni–Mo, or Ni–Au alloy,[18–22] in which the dissolved carbon content is quite sensitive to the thermodynamic process of atomic mixing, in the present approach, all carbon atoms evolving to the final graphene films are precisely controlled by the implantation process in advance. The initial "C-doping" process is decoupled entirely from the complex interdiffusion and precipitation processes. Furthermore, since the final stage of the substrate (on which graphene is formed) is Cu-like (Figure 4a4) and the Ni concentration is negligible, the production of graphene is not affected by the cooling rate (Figure S2, Supporting Information). Therefore, this novel approach is less sensitive to processing conditions such as thermal treatment which would otherwise affect the number of layers of graphene as in other synthesis techniques.

The electrical properties are evaluated using the back-gated graphene field effect transistors (GFETs) prepared by transferring the graphene films onto a 300 nm thick SiO_2/Si substrate. **Figure 6**a shows the schematic diagram and a scanning electron

microscope (SEM) image of the fabricated GFETs. Highly reproducible transport characteristics (I_{DS} $-V_G$) are obtained from both GFETs at room temperature under ambient conditions. The typical I_{DS} $-V_G$ curve acquired at a V_{DS} of 100 mV shows that both hole and electron conduction can be achieved through gating. With regard to the monolayer graphene, the Dirac point of the GFETs locates at a positive gate voltage of $V_G \approx 7$ V (Figure 6b), indicating that the graphene is slightly p-doped. Histogram of the field effect mobility distribution for total 28 devices demonstrates that the monolayer graphene exhibits excellent carrier mobilities in the range of 2500–4000 $cm^2\ V^{-1}\ s^{-1}$ for holes and 1000–3500 $cm^2\ V^{-1}\ s^{-1}$ for electrons, which are comparable to the carrier mobilities reported for monolayer graphene synthesized on metal by CVD.[43,44] For the bilayer graphene, the Dirac point of the GFETs shifts slightly to a positive gate of $V_G \approx 6$ V (Figure 6c). Histogram of the field effect mobility distribution for total 28 devices demonstrates that the bilayer graphene exhibits excellent carrier mobilities in the range of 2000–3500 $cm^2\ V^{-1}\ s^{-1}$ for holes and 1500–3000 $cm^2\ V^{-1}\ s^{-1}$ for electrons. The output characteristics of the GFETs are shown in the right panels of Figure 6b,c. The linear I_{DS} $-V_{DS}$ behavior indicates a good ohmic contact between the Ti/Au contact and graphene channels. In addition, I_{DS} increases with decreasing V_G, suggesting a p-type behavior in the monolayer and bilayer graphene structures. The electrical transport measurements demonstrate that high-quality graphene has been synthesized.

3. Conclusions

In summary, carbon ions are implanted into the Ni/Cu bilayer substrate. Precise control of the carbon content and isothermal precipitation of carbon atoms from the substrate produce graphene layers with the predetermined layer number. Since carbon ion implantation is not thermally driven and completely decoupled from Ni/Cu interdiffusion and carbon precipitation, this technique offers precise control and high flexibility with regard to the choice of the experimental conditions such as annealing parameters. Being compatible with large-scale microelectronics processing, this approach is expected to expedite the application of high-quality graphene to graphene-based nanoelectronic devices.

4. Experimental Section

Graphene Synthesis: The Ni/Cu bilayer substrates were synthesized by depositing a 300 nm thick Ni layer on a high-purity Cu foil (25 μm, Alfa Aesar, Item No. 46365) using an electron beam evaporator. They were implanted with 60 keV carbon ions at fluences of 4×10^{15} and 8×10^{15} atoms cm^{-2} corresponding to the fabrication of monolayer and bilayer graphene films, respectively. The implanted samples were cleaned by acetone, isopropyl alcohol, and deionized water several times to reduce external carbon pollution. Then implanted samples were annealed at 950 °C in Ar and H_2 (200:1 sccm gas flow rate). After annealing, the furnace was cooled to room temperature at the same gas flow rate. The optimal thermal procedures are summarized in Figures S1–S4 (Supporting Information).

Graphene Transfer: After synthesis, the graphene films were transferred by a polymethyl methacrylate (PMMA) -assisted wet-transfer method. The graphene/PMMA film was transferred to water after etching of the Cu–Ni alloy. After removing the PMMA film in acetone, the graphene film was transferred to an oxidized silicon substrate or quartz slides for analysis and characterization. Further experimental details are described in the Supporting Information.

Characterization: Raman scattering (HORIBA Jobin Yvon HR800) was carried out to determine the thickness, quality, and uniformity of the graphene films at room temperature. The Raman spectra were obtained using an Ar^+ laser with a wavelength of 514 nm and a spot size of 1 μm. The spectra were recorded with 600 lines mm^{-1} gratings. Crystallographic information and the number of graphene layers were determined by TEM (FET-Tecnai G2F20 S-7WIN). AFM (Multimode 8) was utilized to determine the uniformity and thickness of the graphene films and STM (Multimode 8) was used to assess the microscopic structure of the graphene films under ambient conditions. After transferring the graphene films onto quartz slides, the optical transmittance spectra were collected on a UV solution u-4100 spectrophotometer. The transmittance properties were determined at a wavelength of 550 nm. The structure of back-gated GFETs was examined by SEM (HITAGHT S-3400N) and XPS (PHI 5802, Physical Electronics Inc., Eden Prairie, MN) was utilized to determine the chemical composition of the sample surface at each stage of the graphene synthesis process. SIMS (Cameca IMS-4F, Paris, France) was performed to obtain the elemental depth profiles using a 7.5 keV Cs^+ beam oriented 70.2° from the sample normal and the detector was positioned 140.4° from the incident beam. The electrical measurements were performed under ambient conditions using an Agilent (B1500A) semiconductor parameter analyzer.

Computational Methods and Models: For the static structure optimization and formation energy calculation, first-principles calculation was performed by the density functional theory (DFT) using the Vienna ab initio simulation package (VASP).[45,46] The electronic exchange and correlation were described by the Perdew–Burke–Ernzerhof (PBE) functional within the generalized gradient approximation (GGA).[47] The spin-polarized projector-augmented wave (PAW) method was used to describe the electronic interaction and the plane-wave kinetic energy cutoff was set as 400 eV. Concerning the static structure optimization and formation energy calculation, the Cu (100) and Ni (100) surfaces are modeled by seven-layer metal slabs with the bottom layer fixed to mimic the half-infinite catalyst structure. The Cu–Ni alloy structures were generated by random substitution of atoms in the host structures. The periodic boundary conditions (PBC) were applied along all three Cartesian directions. A vacuum space larger than 10 Å was applied between neighboring periodic images to avoid the interaction of the adjacent unit cell. The slab model was composed of 4×4 repeating unit cells of Cu (100) and the $2 \times 2 \times 1$ k-point mesh was used in the calculation. All the structures were optimized until the maximum force component on each atom was less than 0.02 eV $Å^{-1}$. In the MD simulation of diffusion of carbon atoms, the Quantum Espresso package[48] was used. The structure models were similar to those described above. The carbon atoms were placed randomly at interstitial positions of the host structures. The structures were then relaxed before MD simulation was carried out at a constant temperature of 1000 K. A small MD time step of 1.2 fs was used to ensure the accuracy of the dynamics. The MSD of carbon atoms is defined as

$$\mathrm{MSD}(t) = \frac{1}{N_C}\sum_{i=1}^{N_c} |\,\vec{r}_i(t) - \vec{r}_i(0)\,|^2 \qquad (2)$$

where N_c is the number of carbon atoms in the model structure and $\vec{r}_i(t)$ is the position of ith carbon atom at time t. The MSD is related to the diffusion coefficient D through the Einstein relationship: $\mathrm{MSD}(t) = 6Dt + C$.

Supporting Information

Supporting Information is available from the Wiley Online Library or from the author.

Acknowledgements

The authors acknowledge the financial support from National Basic Research Program of China (No. 2015CB921600), Creative Research Groups of National Natural Science Foundation of China (No. 61321492), National Natural Science Foundation of China under Grant Nos. 61176001, 51222211, 61006088, 11274222, and 61274136, CAS International Collaboration and Innovation Program on High Mobility Materials Engineering, QiMingXing Project (14QA1402000) from Shanghai Municipal Science and Technology Commission, Eastern Scholar Program and ShuGuang Program (No. 12SG34) from Shanghai Municipal Education Commission, Guangdong – Hong Kong Technology Cooperation Funding Scheme (TCFS) GHP/015/12SZ, and City University of Hong Kong of Strategic Research Grant No. 70041885. Partial support was also provided by the Center for Integrated Nanotechnologies (CINT), a US DOE nanoscience user facility jointly operated by Los Alamos and Sandia National Laboratories. The work at UB was supported by the US Department of Energy under Grant No. DE-SC0002623. The authors also acknowledge High Performance Computing platform of Shanghai University and Shanghai Supercomputer Center.

Received: March 12, 2015
Revised: April 6, 2015
Published online: May 4, 2015

[1] A. K. Geim, K. S. Novoselov, *Nat. Mater.* **2007**, *6*, 183.
[2] A. K. Geim, *Science* **2009**, *324*, 1530.
[3] K. S. Novoselov, V. I. Falko, L. Colombo, P. R. Gellert, M. G. Schwab, K. Kim, *Nature* **2012**, *490*, 192.
[4] H. Li, Q. Zhang, C. Liu, S. H. Xu, P. Q. Gao, *ACS Nano* **2011**, *5*, 3198.
[5] Y. B. Zhang, T. T. Tang, C. Girit, Z. Hao, M. C. Martin, A. Zettl, M. F. Crommie, Y. R. Shen, F. Wang, *Nature* **2009**, *459*, 820.
[6] D. K. Samarakoon, X. Q. Wang, *ACS Nano* **2010**, *4*, 4126.
[7] S. Lee, K. Lee, Z. H. Zhong, *Nano Lett.* **2010**, *10*, 4702.
[8] Q. K. Yu, J. Lian, S. Siriponglert, H. Li, Y. P. Chen, S. S. Pei, *Appl. Phys. Lett.* **2008**, *93*, 113103.
[9] M. E. Ramon, A. Gupta, C. Corbet, D. A. Ferrer, H. P. Movva, G. Carpenter, L. Colombo, G. Bourianoff, M. Doczy, D. Akinwande, E. Tutuc, S. K. Banerjee, *ACS Nano* **2011**, *5*, 7198.
[10] P. W. Sutter, J. I. Flege, E. A. Sutter, *Nat. Mater.* **2008**, *7*, 406.
[11] S. Y. Kwon, C. V. Ciobanu, V. Petrova, V. B. Shenoy, J. Bareno, V. Gambin, I. Petrov, S. Kodambaka, *Nano Lett.* **2009**, *9*, 3985.
[12] Y. W. Wu, G. H. Yu, H. M. Wang, B. Wang, Z. Y. Chen, Y. H. Zhang, B. Wang, X. P. Shi, X. M. Xie, Z. Jin, X. Y. Liu, *Carbon* **2012**, *50*, 5226.
[13] X. S. Li, W. W. Cai, J. H. An, S. Y. Kim, J. H. Nah, D. X. Yang, R. Piner, A. Velamakanni, I. Jung, E. Tutuc, S. K. Banerjee, L. Colombo, R. S. Ruoff, *Science* **2009**, *324*, 1312.
[14] L. B. Gao, W. C. Ren, H. L. Xu, L. Jin, Z. X. Wang, T. Ma, L. P. Ma, Z. Y. Zhang, Q. Fu, L. M. Peng, X. H. Bao, H. M. Cheng, *Nat. Commun.* **2012**, *3*, 699.
[15] B. Kiraly, E. V. Iski, A. J. Mannix, B. L. Fisher, M. C. Hersam, N. P. Guisinger, *Nat. Commun.* **2013**, *4*, 2804.
[16] J. Coraux, A. T. N'Diaye, C. Busse, T. Michely, *Nano Lett.* **2008**, *8*, 565.
[17] G. Wang, M. Zhang, Y. Zhu, G. Q. Ding, D. Jiang, Q. L. Guo, S. Liu, X. M. Xie, P. Chu, Z. F. Di, X. Wang, *Sci. Rep.* **2013**, *3*, 2465.
[18] S. S. Chen, L. Brown, M. Levendorf, W. W. Cai, S. Y. Ju, J. Edgeworth, X. S. Li, C. W. Magnuson, A. Velamakanni, R. D. Piner, J. Y. Kang, J. Park, S. R. Ruoff, *ACS Nano* **2011**, *5*, 1321.
[19] X. Liu, L. Fu, N. Liu, T. Gao, Y. F. Zhang, L. Liao, Z. F. Liu, *J. Phys. Chem. C* **2011**, *115*, 11976.
[20] B. Y. Dai, L. Fu, Z. Y. Zou, M. Wang, H. T. Xu, S. Wang, Z. F. Liu, *Nat. Commun.* **2011**, *2*, 522.
[21] T. Q. Lin, F. Q. Huang, D. Y. Wan, H. Bi, X. M. Xie, M. H. Jiang, *Nanoscale* **2013**, *5*, 5847.
[22] R. S. Weatherup, B. C. Bayer, R. Blume, C. Ducati, C. Baehtz, R. Schlogl, S. Hofmann, *Nano Lett.* **2011**, *11*, 4154.
[23] M. H. Rümmeli, M. Q. Zhen, S. Melkhanova, S. Gorantla, A. Bachmatiuk, L. Fu, C. L. Yan, S. Oswald, R. G. Mendes, D. Makarov, O. Schmidt, J. Eckert, *Chem. Mater.* **2013**, *25*, 3880.
[24] Y. P. Wu, H. Chou, H. X. Ji, Q. Z. Wu, S. S. Chen, W. Jiang, Y. F. Hao, J. Y. Kang, Y. J. Ren, R. D. Piner, R. S. Ruoff, *ACS Nano* **2012**, *6*, 7731.
[25] D. Y. Wan, T. Q. Lin, H. Bi, F. Q. Huang, X. M. Xie, I. W. Chen, M. H. Jiang, *Adv. Funct. Mater.* **2012**, *22*, 1033.
[26] S. Garaj, W. Hubbard, J. A. Golovchenko, *Appl. Phys. Lett.* **2010**, *97*, 183103.
[27] L. Baraton, Z. B. He, C. S. Lee, J. L. Maurice, C. S. Cojocaru, A. F. Gourgues-Lorenzon, Y. H. Lee, D. Pribat, *Nanotechnology* **2011**, *22*, 085601.
[28] G. Wang, G. Q. Ding, Y. Zhu, D. Chen, L. Ye, L. Zheng, M. Zhang, Z. F. Di, S. Liu, *Mater. Lett.* **2013**, *107*, 170.
[29] J. S. Lee, C. W. Jang, J. M. Kim, D. H. Shin, S. Kim, S. H. Choi, K. Belay, R. G. Elliman, *Carbon* **2014**, *66*, 267.
[30] L. Baraton, Z. B. He, C. S. Lee, C. S. Cojocaru, M. Chatelet, J. L. Maurice, Y. H. Lee, D. Pribat, *Europhys. Lett.* **2011**, *96*, 46003.
[31] J. F. Ziegler, M. D. Ziegler, J. P. Biersack, *Nucl. Instrum. Methods Phys. Res., Sect. B* **2010**, *268*, 1818.
[32] P. Zhao, S. J. Kim, X. Chen, E. Einarsson, M. Wang, Y. N. Song, H. T. Wang, S. Chiashi, R. Xiang, S. Maruyama, *ACS Nano* **2014**, *8*, 11631.
[33] Z. Yan, J. Lin, Z. W. Peng, Z. Z. Sun, Y. Zhu, L. Li, C. S. Xiang, E. L. Samuel, C. Kittrell, J. M. Tour, *ACS Nano* **2012**, *6*, 9110.
[34] A. C. Ferrari, D. M. Basko, *Nat. Nanotechnol.* **2013**, *8*, 235.
[35] R. R. Nair, P. Blake, A. N. Grigorenko, K. S. Novoselov, T. J. Booth, T. Stauber, N. M. Peres, A. K. Geim, *Science* **2008**, *320*, 1308.
[36] Z. Z. Sun, A. R. Raji, Y. Zhu, C. S. Xiang, Z. Yan, C. Kittrell, E. L. Samuel, J. M. Tour, *ACS Nano* **2012**, *6*, 9790.
[37] J. Hofrichter, B. N. Szafranek, M. Otto, T. J. Echtermeyer, M. Baus, A. Majerus, V. Geringer, M. Ramsteiner, H. Kurz, *Nano Lett.* **2010**, *10*, 36.
[38] G. M. Rutter, S. Y. Jung, N. N. Klimov, D. B. Newell, N. B. Zhitenev, J. A. Stroscio, *Nat. Phys.* **2011**, *7*, 649.
[39] K. Yan, H. L. Peng, Y. Zhou, H. Li, Z. F. Liu, *Nano Lett.* **2011**, *11*, 1106.
[40] J. Hwang, M. Kim, D. Campbell, H. A. Alsalman, J. Y. Kwak, S. Shivaraman, A. R. Woll, A. K. Singh, R. H. Hennig, S. Gorantla, M. K. Rummeli, M. G. Spencer, *ACS Nano* **2013**, *7*, 385.
[41] A. Dimiev, D. V. Kosynkin, A. Sinitskii, A. Slesarev, Z. Z. Sun, J. M. Tour, *Science* **2011**, *331*, 1168.
[42] S. Amini, J. Garay, G. X. Liu, A. A. Balandin, R. Abbaschian, *J. Appl. Phys.* **2010**, *108*, 094321.
[43] W. Liu, H. Li, C. Xu, Y. Khatami, K. Banerjee, *Carbon* **2011**, *49*, 4122.
[44] A. Reina, X. T. Jia, J. Ho, D. Nezich, H. Son, V. Bulovic, M. S. Dresselhaus, J. Kong, *Nano Lett.* **2009**, *9*, 30.
[45] G. Kresse, J. Furthmüller, *Comput. Mater. Sci.* **1996**, *6*, 15.
[46] G. Kresse, J. Furthmüller, *Phys. Rev. B* **1996**, *54*, 11169.
[47] J. P. Perdew, K. Burke, M. Ernzerhof, *Phys. Rev. Lett.* **1996**, *77*, 38658.
[48] P. Giannozzi, S. Baroni, N. Bonini, M. Calandra, R. Car, C. Cavazzoni, D. Ceresoli, G. Chiarotti, M. Cococcioni, I. Dabo, A. D. Corso, S. D. Gironcoli, S. Fabris, G. Fratesi, R. Gebauer, U. Gerstmann, C. Gougoussis, A. Kokalj, M. Lazzeri, L. Martin-Samos, N. Marzari, N. Mauri, N. Mazzarello, S. Paolini, A. Pasquarello, L. Paulatto, C. Sbraccia, S. Scandolo, G. Sclauzero, A. P. Seitsonen, A. Smogunov, P. Umari, R. M. Wentzcovitch, *J. Phys.: Condens. Matter* **2009**, *21*, 395502.